BNL-96480-2011-JA

EXTENSION OF WRF TO CLOUD-RESOLVING SIMULATIONS DRIVEN BY LARGE-SCALE AND SURFACE FORCINGS

PART I: MODEL CONFIGURATION AND VALIDATION

Satoshi Endo*, Yangang Liu, Wuyin Lin, and Gang Liu

**Corresponding author: Satoshi Endo, Brookhaven National Laboratory, Bldg. 815E, 75 Rutherford Dr., Upton, NY 11973, USA; E-mail: sendo@bnl.gov*

Submitted to Monthly Weather Review

October 2011

Atmospheric Sciences Division/Environmental Sciences Dept.

Brookhaven National Laboratory

U.S. Department of Energy
Office of Science

DISCLAIMER

Abstract

As a community model the Weather Research and Forecasting (WRF) model has been applied to the simulations of boundary layer and cloud processes in nested or idealized settings. We have further extended the capability of the WRF model to simulate clouds that are driven by time-varying large-scale and surface forcings. This paper describes the newly configured WRF-LES and validates its performance in comparison with well-established LES models. Two different benchmark simulations from the Global Energy and Water Cycle Experiment (GEWEX) Cloud System Study (GCSS) intercomparisons are used in the evaluation: quasi-steady maritime stratocumulus clouds from the second research flight of the second Dynamics and Chemistry of Marine Stratocumulus field study (DYCOMS-II RF02) and evolving continental cumulus clouds at the Atmospheric Radiation Measurement Southern Great Plains site (ARM SGP). For the DYCOMS-II RF02 case, the newly configured WRF-LES simulates stratocumulus clouds in quasi-equilibrium state as in other LES models, with most cloud properties having values close to the ensemble mean of the other models. For the ARM SGP case, the shallow cumulus clouds produced by the newly configured WRF-LES have nearly identical properties to those simulated by the KNMI-LES model in terms of the diurnal variation and vertical profiles of mean state and turbulent fluxes. Difference between the two models is only 10% in cloud mass flux and less than 1% in cloud core mass flux at cloud base. The favorable agreement with existing LES models lend credence to the newly configured WRF as a community large-eddy simulation or cloud-resolving model driven by either fixed or time-varying large-scale forcings.

1. Introduction

Large-eddy simulation (LES) and cloud-resolving models (CRM) have been widely used to study a variety of atmospheric phenomena ranging from boundary layer turbulence and cloud processes (e.g., Deardorff 1972; Moeng 1984; Moeng 1986; Stevens et al. 1998; Brown et al. 2002; Siebesma et al. 2003) to the evolution of tropical and midlatitude continental convective cloud systems (e.g., Grabwoski et al. 1996; Wu and Moncrieff 2001; Xu and Randall 2001; Khairoutdinov and Randall 2003; Wu and Li 2008; Tao and Moncrieff 2009).

In addition to their conventional role, LES and CRM are increasingly being recognized as an essential tool for evaluating and developing parameterizations of subgrid processes in numerical weather prediction and climate models (Randall et al. 2003b). The improvement of cloud-related parameterizations is important since representation of cloud and precipitation processes have significant consequence on the quality of weather forecasting and climate simulations. One of the approaches to this problem is to utilize LES/CRM as a virtual laboratory to provide dataset needed for constructing and evaluating the parameterization but difficult to be obtained from observations. Compared with the grid spacing of the current climate models (horizontal resolution $\Delta h \sim 100$ km), LES and CRM use finer grid spacing ($\Delta h \sim$ few - 100 m for LES and $\leq$ few km for CRM) to explicitly simulate energetic eddies and clouds with less parameterizations.

In the past few decades, many efforts have been made to improve the parameterizations in the climate models (Randall et al. 2003a). In particular, the Global Energy and Water Cycle Experiment (GEWEX) Cloud System Study (GCSS) program

(Browning et al. 1993; Randall et al. 2003b) have been performing model intercomparison studies based on observational cases. The activity of the boundary layer cloud working group has shown the values of LES/CRM in providing advanced understanding on cloud-topped boundary layers (e.g., Stevens et al. 2001; Siebesma et al. 2003; Stevens et al. 2005; Brown et al. 2002; Ackerman et al. 2009). The GCSS cases have also been used for the examination of single column model (SCM) simulations, which represents a grid column of a climate model (e.g., Duynkerke et al. 2004; Lenderink et al. 2004; Wyant et al. 2007; Zhu et al. 2005). Driven by the same forcing, LES/CRM results can also provide information on subgrid variability needed for further improving fast physics parameterizations in SCM (GCM).

The Advanced Research version of Weather Research and Forecasting model (WRF-ARW) is a compressible nonhydrostatic model which has been developed at National Center for Atmospheric Research (NCAR) in collaboration with several institutes and universities for operational weather forecasting and atmospheric science research (Skamarock et al. 2008). Although the primary focus of WRF is on meso-scale to synoptic-scale convection, there have been some attempts to extend WRF to perform cloud-resolving and large-eddy simulations. Moeng et al. (2007) recently explored the possibility of using WRF as a LES model (WRF-LES) to study dry boundary layer convection. They performed a high-resolution LES nested within a low-resolution LES, and compared it to an LES using doubly periodic boundary conditions. Although there was still issues associated with the treatment of lateral boundaries, the nested LES was shown to be able to simulate the turbulent eddies as the idealized LES did. Since then, the nested WRF-LES has began to be used for the researches on wind energy prediction

(Liu et al. 2011b; Lundquist et al. 2008) and boundary layer processes under realistic environments (Zhu 2008; Zhu et al. 2010). In addition to the nested WRF-LES, a few studies also explored the potential of using WRF as an LES model under idealized settings to investigate dry boundary layers (Catalano and Moeng 2010; Liu et al. 2011a) and cellular cloud structures (Wang and Feingold 2009a, 2009b) .

Although previous studies have demonstrated the potential of using WRF to simulate clouds and turbulent eddies, still lacking in current WRF is a full consideration of time-varying large-scale forcing, a function of typical CRM and LES that has proven essential for more realistic cloud-resolving and large-eddy simulations and parameterization development. For example, performing CRM/LES simulations together with single column model (SCM) driven by the same large-scale forcing has been a primary strategy used in programs aiming at improving cloud parameterizations in large-scale models [e.g., GCSS, Atmospheric Radiation Measurement (ARM, Stokes and Schwartz 1994; Ackermann and Stokes 2003), and now Atmospheric System Research (ASR)]. A similar strategy is also adopted by the latest FAst-physics System TEstbed and Research (FASTER) project supported by the Department of Energy Earth System Modeling (ESM) Program.

Under the FASTER project, we have further extended the WRF's capability to allow for flexible consideration of time-varying large-scale and surface forcings in cloud-resolving and large-eddy simulations. The objectives of this paper are to introduce the major functions and modifications of the newly configured WRF-LES (referred to as WRF-FASTER hereafter), and to provide validation by comparing its performance with well-established LES models in simulating well-studied cases.

The rest of this paper is organized as follows. Section 2 describes the implementation of the external forcing into WRF-LES and configurations of the simulations for the two GCSS cases. The WRF-FASTER simulations are evaluated against other LES models in Section 3. The major results are summarized in Section 4.

2. Model configuration and simulation setup

a. Implementation of external forcing

The surface and large-scale forcings are introduced as external forcings that are prescribed and considered as source or sink of heat and moisture instead of being calculated in model dynamics or physics schemes. The surface forcing consists of sensible and latent heat fluxes from surface. The large-scale forcing represents the effect of three-dimensional advection of heat and moisture by larger scale motions to the model domain.

Under the assumption that spatial variation of large-scale variable is small (Siebesma and Cuijpers 1995; Grabowski et al. 1996), the large-scale advective tendencies for potential temperature θ and water vapor mixing ratio q_v are written as

$$\left(\frac{\partial \overline{\theta}}{\partial t}\right)_{\mathrm{LS}} = -\bar{\mathbf{v}} \cdot \boldsymbol{\nabla}\bar{\theta} - \overline{w}\frac{\partial \bar{\theta}}{\partial z} \tag{1}$$

and

$$\left(\frac{\partial \overline{q_v}}{\partial t}\right)_{\mathrm{LS}} = -\bar{\mathbf{v}} \cdot \boldsymbol{\nabla}\overline{q_v} - \overline{w}\frac{\partial \overline{q_v}}{\partial z} \tag{2}$$

where LS is denotation of large scale, $\mathbf{v} = (u, v)$ is horizontal wind velocity, w is vertical wind velocity; the overbar denotes large-scale mean. A physical quantity φ can be expressed as $\varphi = \varphi' + \overline{\varphi}$, with φ' representing cloud scale perturbation. The

first and second terms in right hand side represent large-scale horizontal and vertical advections, respectively.

For this simulation, the effect of the large-scale advection is represented as additional terms in the governing equations in the model:

$$\left(\frac{\partial\theta}{\partial t}\right)_{\mathrm{LS}} = -\mathbf{V}\cdot\boldsymbol{\nabla}\Theta - W\frac{\partial\theta}{\partial z} \tag{3}$$

and

$$\left(\frac{\partial q_v}{\partial t}\right)_{\mathrm{LS}} = -\mathbf{V}\cdot\boldsymbol{\nabla}Q_v - W\frac{\partial q_v}{\partial z} \tag{4}$$

where capital variables (Θ, Q_v, $\mathbf{V}$ and W) represent large-scale fields associated with external forcing in order to distinguish from the prognostic variables in the model (indicated by the small letters (θ, q_v, $\mathbf{v}$ and w). Whereas the horizontal advection term and W in the vertical advection term are prescribed in the external file, we use the vertical gradient of local value $\partial\theta/\partial z$ and $\partial q_v/\partial z$ with the assumption that

$$\frac{\partial\overline{\theta}}{\partial z} = \overline{\frac{\partial\theta}{\partial z}} \quad \text{and} \quad \frac{\partial\overline{q_v}}{\partial z} = \overline{\frac{\partial q_v}{\partial z}}\ . \tag{5}$$

Another major approach to implement the large-scale forcing is relaxation of the prognostic variables to reference values, using the following equations:

$$\left(\frac{\partial\theta}{\partial t}\right)_{\mathrm{R}} = \frac{\Theta-\overline{\theta}}{\tau} \quad \text{and} \quad \left(\frac{\partial q_v}{\partial t}\right)_{\mathrm{R}} = \frac{Q_v-\overline{q_v}}{\tau} \tag{6}$$

for scalars, and

$$\left(\frac{\partial u}{\partial t}\right)_{\mathrm{R}} = \frac{U-\overline{u}}{\tau} \quad \text{and} \quad \left(\frac{\partial v}{\partial t}\right)_{\mathrm{R}} = \frac{V-\overline{v}}{\tau} \tag{7}$$

for momentum. Here R denotes relaxation, and τ is the relaxation time. The relaxation is often used as the large-scale forcing terms for u and v, and sometimes as additional terms to constrain θ and q_v. Although relaxations of these variables as a

way to implement large-scale forcing has been implemented in WRF-FASTER as an alternative, its validation and evaluation are left to Part II of this series.

In addition to the large-scale forcing, a function to prescribe time-varying surface sensible and latent heat fluxes was implemented and applied in this study to follow the case specifications. The surface sensible and latent heat fluxes are supplied to the lowest layer of the atmosphere in the model. Some other surface parameters were also specified as described later.

b. Simulated cases and model setup

Two GCSS cases are chosen to test the ability of WRF-FASTER. One represents maritime stratocumulus clouds based on the second research flight (RF02) of Second Dynamics and Chemistry of Marine Stratocumulus field study (DYCOMS-II; Stevens et al. 2003) as described in Ackerman et al. (2009); the other represents continental shallow cumulus clouds collected at the Southern Great Plains (SGP) site of ARM, which is described in Brown et al. (2002). Both cases have been well investigated in previous model intercomparison studies, and results from these studies are available as references for comparison with the WRF-FASTER simulations. In our simulations, all the configurations followed the case specifications for the intercomparison studies except the vertical resolution because WRF applies a normalized pressure vertical coordinate (see below for more information). More information about these cases can be found in Ackerman et al. (2009) for the DYCOMS-II RF02 case and Brown et al. (2002) for the ARM SGP case.

1) THE DYCOMS-II RF02 CASE

The DYCOMS-II RF02 case represents nocturnal stratocumulus clouds in quasi-steady state over ocean derived from the RF02 flight collected during the DYCOMS-II field campaign conducted off the coast of California in July 2001.The DYCOMS-II RF02 case applies constant surface and large-scale forcings with a simple long-wave radiation scheme. The case imposes constant sensible heat flux of 16 W m^{-2}, latent heat flux of 93 W m^{-2} and surface friction velocity of 0.25 m s^{-1}. Large-scale subsidence is specified as $W = Dz$ with a constant divergence $D = 3.75 \times 10^{-6}$ s^{-1}. The large-scale vertical advection of heat and moisture are then calculated using the Eqs. 3 and 4. Large-scale horizontal advection is not considered in this case.

The model domain is 6.4 km × 6.4 km × 1.5 km with 128 × 128 × 200 grid points. While the horizontal resolution is 50 m, the vertical grid spacing doesn't follow the specification. Since WRF employs hydrostatic pressure vertical coordinate [$\eta = (p_h - p_{ht})/(p_{hs} - p_{ht})$ where p_h is hydrostatic component of pressure, p_{ht} and p_{hs} are those at model top and surface, respectively], uniform η spacing is used for vertical grids of which an average vertical resolution in physical height is 7.5 m. Sponge layer is applied above 1250 m for gravity wave absorption.

For the DYCOMS-II RF02 case, specific radiation scheme and cloud water sedimentation scheme are used (see Appendix for detailed information on radiation scheme, sedimentation scheme and the initial condition). Lin et al. (1983) scheme is modified to include cloud water sedimentation in the Stokes regime. Number concentration of cloud droplets is set to 50 cm^{-3}. Radiative transfer is computed using the parameterization in Stevens et al. (2005), which considers long wave radiation from

liquid water and balance between subsidence heating and radiative cooling. Prognostic TKE scheme (Deardorff 1980) is used for subgrid-scale turbulence.

The initial conditions for potential temperature and water vapor mixing ratio are determined based on the specified profiles of liquid water potential temperature and total water mixing ratio (Appendix and thin lines in Fig. 4). The liquid water potential temperature is written as

$$\theta_l \simeq \theta - \frac{L_v\, q_l}{\pi\, c_p} \qquad (8)$$

where L_v is the latent heat of vaporization of water, q_l is liquid water mixing ratio, $\pi \equiv (p/p_0)^{R_d/C_p}$ is the Exner function, c_p is the specific heat at constant pressure, and R_d is the gas constant for dry air. Random potential temperature perturbation and initial TKE were given to initiate turbulence smoothly. The simulation continued for a total of 6 hours in integration.

2) THE ARM SGP CASE

The ARM SGP case represents a typical diurnal evolution of shallow cumulus clouds over land. The case is an idealization based on the sounding and surface flux observations on 21 June 1997 at the ARM SGP site.

A time-varying, horizontally uniform surface flux and large-scale forcing of heat and moisture are applied to the ARM SGP case. Figure 1 shows the time variation of prescribed surface sensible and latent heat fluxes. The surface fluxes show strong diurnal variation with its peaks between 12 and 13 local time (LT = UTC - 6). Table 1 shows the specified large-scale advective forcing of heat and moisture, as well as radiative heating. The sum of the radiative and advective heatings is considered as the

total large-scale forcing of heat. The large-scale forcings are constant with height below 1000 m and linearly decreased to zero between 1000 and 2000 m. The vertical profiles of the large-scale forcing of heat and moisture were linearly interpolated into every time steps in the simulation. The forcing terms were then added to the tendency equations as in Eqs. 3 and 4. Large-scale vertical motion is not applied to this case.

While the horizontal grid spacing is 66.7 m as specified in Brown et al. (2002), vertically uniform η spacing is applied so that the average vertical resolution is 40 m. The domain size is 6.4 km × 6.4 km × 4.4 km consisting of 96 × 96 × 110 grid points. Sponge layer is applied above 3500 m for damping gravity wave.

In simulation of the ARM SGP case, all physics schemes are selected from the standard WRF: prognostic TKE scheme (Deardorff 1980) for subgrid scale turbulence closure, Lin et al. (1983) scheme for cloud microphysics. Although the bottom boundary conditions for heat and moisture have been specified as the surface sensible and latent heat fluxes, friction velocity for the momentum is computed in the MM5 surface layer scheme using the Monin-Obukhov similarity with the roughness length of 0.035 m. Radiation scheme was turned off for the ARM SGP case because the specified large-scale forcing includes the effect of the radiative heating.

The simulation is initialized with the stratified potential temperature and moisture (thin lines in Figs. 9), and meridional wind of 10 m s^{-1}. Initial perturbations are applied to potential temperature and TKE. The integration continued for a period of 15 hours between 0530 and 2030 LT to simulate the daytime evolution of the cumulus-topped boundary layer.

3. Result

a. Maritime stratocumulus clouds

Figure 2 shows time-height variation of virtual potential temperature, variance of vertical velocity, water vapor and cloud fraction for the WRF-FASTER simulation of the DYCOMS-II RF02 case. Integration time (IT, in hours) is used as a scale of time in the figures, because this case applied "perpetual night" configuration that included no time variation in the surface and large-scale forcing in order to achieve the equilibrium state. From the beginning of the simulation, the cloud fraction shows existence of solid cloud deck in the upper half of the boundary layer below the strong inversion. At 01 IT, the cloud deck is coupled with the dry convection in the sub-cloud layer, which is found to have large variance of vertical velocity. After 2 hours of spin-up (02 IT), stratocumulus clouds vary little with time until the end of the simulation, suggesting that the simulated stratocumulus cloud is maintained at quasi-steady state as expected.

This DYCOMS-II RF02 case was investigated by 13 LES models in a recent model intercomparison study (Ackerman et al. 2009). As references, these model results are compared with the WRF-FASTER simulations. Figure 3 compares the time series of major cloud properties. Cloud top is defined as the mean height of the isosurface of total water q_t = 8 g kg^{-1} in the inversion layer. Total cloud fraction is defined as the fraction of model columns with liquid water path larger than 70 mm. Both cloud top and base heights increase slightly with time in the WRF-FASTER simulation as in the other models' simulations. The total cloud fraction and liquid water path of WRF-FASTER are slightly lower than the ensemble mean, but still close to the

center of the ensemble range. The maximum variance of vertical velocity fluctuates around the ensemble mean, but stays within the ensemble range.

Figure 4 further compares the vertical profiles of clouds and thermodynamic properties for the DYCOMS-II RF02 case. The vertical profile represents the average over the final 4 hours (02 - 06 IT) of the quasi-steady state. Evidently, all the models produce virtually the same vertical profiles of potential temperature and water vapor (Figs. 4a and 4b). The liquid water mixing ratio and cloud fraction of WRF-FASTER (Figs. 4c and 4d) are close to the ensemble mean, except for the smaller values near the cloud base. Even near the cloud base, the WRF-FASTER results still fall within the range of the ensemble. The vertical fluxes of liquid water potential temperature and total water exhibit relatively large differences from the ensemble means (Figs. 4e and 4f). The liquid water potential temperature flux is generally smaller than the ensemble range whereas the total water flux is larger than the ensemble mean on average. Also shown in Fig. 4 are the corresponding initial vertical profiles (thin lines). Compared to the initial condition, the inversion is slightly higher, and the subcloud layer is slightly warmer and moister in all the models.

As shown in Fig. 4, the liquid water potential temperature flux is smaller in the WRF-FASTER than the ensemble mean whereas the opposite is true for the total water flux. In the WRF-FASTER simulation, the surface liquid water potential temperature flux and total water flux (16.7 and 95.3 W m^{-2}) are similar to the imposed surface sensible and latent heat fluxes (16 and 93 W m^{-2}). This implies that the contribution of precipitation is much smaller in WRF-FASTER compared to the other models. To support this speculation, Figure 5 compares the rain water amount and precipitation flux

simulated by WRF-FASTER and the other models. As expected, the smallest rain water amount of WRF-FASTER is close to the lower end of the inter-model spread. The small rain water amount results in a small precipitation flux below cloud base, leading to the difference in the total water flux. The small precipitation flux can also contribute to the small liquid water potential temperature flux as follows. Liquid water potential temperature flux can be decomposed into two components given by:

$$\overline{w'\theta_l'} = \overline{w'\theta'} - \frac{L_v}{\pi c_p}\overline{w'q_l'} \qquad (10)$$

where the first term on the right hand side $\overline{w'\theta'}$ is the flux of potential temperature and $\overline{w'q_l'}$ in the second term is the flux of liquid water (Siebesma et al. 2003). Moreover, the liquid water flux consists of the resolved-scale transport of liquid water and subgrid-scale sedimentation flux. Figure 6 shows the liquid water potential temperature flux and its various components. Figure 6 implies that the increase in the sedimentation flux can lead to the increase in the contribution of liquid water flux, and produce the larger liquid water potential temperature flux. As shown in Fig. 5, the rain water amount is the variable that exhibits the largest spread among the models. These results suggest that the more apparent differences in the vertical fluxes are due likely to the rain water production associated with the microphysical parameterization. Investigation of microphysics process with the focus on the precipitation efficiency is necessary.

b. Continental shallow cumulus clouds

One of the extended capabilities of WRF-FASTER is its objective use of time-varying large-scale forcing and surface fluxes to drive the simulation. To demonstrate this

capability, the WRF-FASTER simulation of diurnal evolution of the continental shallow cumulus clouds is examined. Figure 7 shows time height section of horizontally averaged virtual potential temperature, variance of vertical motion, water vapor mixing ratio and cloud fraction from the WRF-FASTER simulation of the ARM SGP case. The cloud fraction at each altitude is defined as the fraction of grid boxes in which cloud condensate is larger than 0.01 g kg^{-1}. Formation of the first cumulus cloud takes place around 09 LT (Fig. 7a), following the formation of the dry convective boundary layer, which appears as small vertical gradient of virtual potential temperature and large variance of vertical motion near the surface (Fig. 7b). In the subcloud layer, water vapor is well mixed by the dry convection indicated by the variance of vertical velocity. The cumulus clouds forms the cloud layer in which virtual potential temperature and water vapor profile have larger gradient than in the underlying subcloud layer. The cloud layer continues to develop until around 18 LT, at which time the surface flux becomes small and the clouds start to be dissipated.

The cloud properties simulated by WRF-FASTER are compared with those by the KNMI-LES, developed at Royal Netherlands Meteorological Institute (Cuijpers and Duynkerke 1993). Figure 8 shows time variation of the maximum height of cloud top, the minimum height of cloud base, total cloud fraction, maximum cloud fraction, and liquid water path of cumulus clouds simulated by WRF-FASTER and KNMI-LES. Note that, to be consistent with the reference data from the previous intercomparison study, total cloud fraction is differently defined in Fig. 3 and Fig. 8. The total cloud fraction here is defined as the fraction of model columns with cloud condensate larger than 0.01 g kg^{-1}. The total cloud fraction in Figure 3 is defined as the fraction of model

columns with liquid water path larger than 70 mm. The maximum cloud fraction is the maximum value in the vertical profile of the cloud fraction, which is found at cloud base height for cumulus clouds. It is clear that WRF-FASTER compares favorably with KNMI-LES in the cloud properties examined here. In both simulations, the increase rate of the maximum cloud top height is large until 14 LT, and small between 14 and 18 LT (Fig. 8a). The gradually increasing cloud base is slightly lower in WRF-FASTER than in KNMI-LES, though the difference is less than 100 m. Contrasting to the increasing thickness of the cloud layer, the total and maximum cloud fractions peak between 11 and 12 LT, and then gradually decrease with time (Fig. 8b). The local noon time (12 LT), likely corresponds to the onset of buoyant cumulus (active cumulus) clouds. Liquid water path shows large value in early afternoon with a short break around 14 LT (Fig. 8c). The short break in liquid water path is likely caused by evaporation of cloud water due to the entrainment of dry air from free atmosphere, because at 14 LT the cloud top reaches the dry layer above the 2500 m as shown in Fig. 7a. Despite the large diurnal variation, the cumulus clouds produced by WRF-FASTER are quantitatively similar to those in KNMI-LES including some key transitions: the first cumulus occurrence, the active cumulus onset, the short break in liquid water path, and dissipation in evening. Relative difference to the KNMI-LES at 12 LT is -158 m (64m) in cloud top (base) height, -0.026 (0.001) in total (maximum) cloud fraction, and 1.82 mm in liquid water path, which is smaller than the amplitude of fluctuation in the each model.

Figure 9 shows the vertical profiles of cloud and thermodynamic properties averaged over the period between 12 and 13 LT in the ARM SGP case. As described above, the simulation initialized by the stable profile has evolved with time. For the

potential temperature and water vapor (Figs. 9a and 9b), the profiles of WRF-FASTER virtually overlap those of KNMI-LES. The changes in potential temperature and water vapor correspond to the structure consisting of the subcloud layer lower than 900 m and the cloud layer between 900 and 2100 m (Figs. 9c and 9d). The cloud core fraction are defined by the ratio of cloudy, buoyant grids ($q_c > 0.01$ g kg^{-1} and $\theta_v' > 0$) to the total number of grids at a certain height. Compared to KNMI-LES, WRF-FASTER shows slightly smaller cloud fraction. The cloud core fractions in both simulations agree well with each other.

The cumulus topped boundary layer evolves as a result of the liquid water potential temperature flux and total water flux shown in the Figs. 9e and 9f. In addition to resolved fluxes explicitly calculated from grid-scale variables, the total fluxes shown here take into account the subgrid-scale diffusion computed in the turbulence scheme. In the ARM SGP case, the contribution from rain water falling at terminal velocity is negligibly small compared to the resolved flux. The subgrid-scale turbulent flux is dominant only at the lowest few model levels, and most of the transport of energy and water is caused by the resolved turbulent motion. Both simulations show a convergence of the liquid water potential temperature flux below 1300 m and divergence between 1300 and 2200m. The total water flux indicates vigorous moistening around the top of the cloud layer. The vertical fluxes in the WRF-FASTER simulation shows typical feature of cumulus topped boundary layer, which also can be found in the KNMI-LES simulation.

The evaluation is extended to cloud-mass flux in view of its seminal role in parameterizing the vertical transport by convection (e.g., Neggers et al. 2004; Soares et al. 2004; Siebesma et al. 2007). The cloud mass flux is defined by

$$M_c \equiv \overline{w}^c A_c \qquad (9)$$

where $\overline{w}^c$ is the vertical velocity averaged over cloudy grid boxes ($q_c > 0.01$ g kg^{-1}), and A_c is the area occupied by cloudy grid boxes. For cloud core mass flux, cloudy and buoyant grid boxes ($q_c > 0.01$ g kg^{-1} and $\theta_v' > 0$) are used instead of cloudy grid boxes.

Figure 10 compares the vertical profiles of mass fluxes calculated from the outputs of WRF-FASTER and KNMI-LES. The cloud mass flux is 10% larger in WRF-FASTER than in KNMI-LES; the difference in cloud core mass flux is much less ($< 1\%$) between the two models. According to Brown et al. (2002), these model differences are smaller than the inter-model spread among the cloud-resolving and large-eddy simulation models participating in the model comparison. The result suggests that WRF-FASTER is capable of generating cloud scale dynamics for assessing/improving mass flux based cumulus parameterization schemes.

4. Concluding Remark

The capability of the WRF-ARW model has been extended by implementing functions to consider general large-scale and surface forcings, including both fixed and time-varying forcings. This extension enables the newly configured WRF (WRF-FASTER) to be used as a community CRM or LES. The performance of WRF-FASTER has been evaluated through two different benchmark simulations from the GCSS intercomparison

cases: the DYCOMS-II RF02 case for quasi-steady maritime stratocumulus clouds and the ARM SGP case for evolving continental cumulus clouds.

For the DYCOMS-II RF02 case, quasi-steady stratocumulus clouds are simulated by the WRF-FASTER, at least equally well as the other 13 models participating in the model intercomparison. Relatively smaller (larger) liquid water potential temperature (total water) flux in WRF-FASTER can be explained by smaller rain water production in the microphysics scheme. These results indicate that the relative difference between the WRF-FASTER and the ensemble mean of other LES models arises likely from the microphysics scheme used in the current WRF-FASTER simulations, not the WRF-FASTER per se. This topic warrants further investigation in the future.

Driven by the time-evolving forcings, WRF-FASTER successfully simulates the diurnal variation of cumulus clouds in the ARM SGP case. Diurnal variation and vertical profiles of mean state and vertical fluxes produced by WRF-FASTER are quantitatively similar to those simulated by the well-tested KNMI-LES model. The overall favorable agreement with existing LES model lend strong credence to using WRF-FASTER as a community cloud-resolving or large-eddy simulation model driven by either fixed or time-varying large-scale forcings.

It is noteworthy that the newly implemented functions in WRF-FASTER can consider more general large-scale and surface forcings than the cases reported in this study. For example, ARM provides long-term continuous large-scale forcing data (Zhang et al. 2001; Xie et al. 2004) along with a suite of other observations that are essential to evaluate cloud-related parameterizations. Application of WRF-FASTER

driven by the continuous large-scale forcing to simulate the observed clouds and precipitation by ARM will be reported in Part II of this series.

Acknowledgement

This research is supported by the U.S. Department of Energy Earth System Modeling (ESM) program via the FASTER project (www.bnl.gov/esm). The research utilized resources at the New York Center for Computational Sciences.

APPENDIX

Initial profile, radiative transfer, and cloud water sedimentation for the DYCOMS-II RF02 case

a) Initial profile

The horizontally uniform initial condition was generated by the following equations:

$$u = 3 + 4.3\, z \,/\, 1000 \tag{11}$$

and

$$\upsilon = -9 + 5.6\, z \,/\, 1000 \tag{12}$$

for horizontal wind components,

$$\theta_l = \begin{cases} 288.3 & (z < z_i) \\ 295 + (z - z_i)^{1/3} & (z \geq z_i) \end{cases} \tag{13}$$

and

$$q_t = \begin{cases} 9.45 & (z < z_i) \\ 5 - 3\left[1 - \exp\left(\frac{z_i - z}{500}\right)\right] & (z \geq z_i) \end{cases} \tag{14}$$

for liquid water potential temperature θ_l and total water mixing ratio q_t, where z_i = 795 m is inversion height.

b) Radiative transfer

Radiative transfer was calculated by the scheme in Stevens et al. (2005):

$$\begin{aligned} F(z) = {} & F_0 \exp[-Q(z,\infty)] + F_1 \exp[-Q(0,z)] \\ & + \alpha\, \rho_l\, c_p\, D\mathrm{H}(z - z_i)\left[0.25(z - z_i)^{4/3} + z_i(z - z_i)^{1/3}\right] \end{aligned} \tag{15}$$

where F_0 = 70 W m^{-2}, F_1 = 22 W m^{-2}, a = 1 K m$^{1/3}$, ρ_l = 1.12 g m^{-3}, c_p =1004 J kg^{-1}K^{-1}, $D = 3.75 \times 10^{-6}$, H(x) = 0 when $x < 0$ otherwise 1, κ = 85 m^2 kg^{-1}, z_i is inversion height defined by the minimum height at which q_t = 8 g kg^{-1} in the vertical column.

c) Cloud water sedimentation

With the assumption of a lognormal size distribution of droplet falling in the Stokes regime, cloud water sedimentation flux was calculated by

$$F = c \left(\frac{3}{4 \pi \rho_l N}\right)^{5/3} \exp(5 \ln^2 \sigma_g) \qquad (17)$$

where $c = 1.19 \times 10^8$ m^{-1} s^{-1}, standard deviation $\sigma_g = 1.5$, number concentration N = 55 cm^{-3}.

References

Ackerman, A. S., and Coauthors, 2009: Large-eddy simulations of a drizzling, stratocumulus-topped marine boundary layer. *Mon. Wea. Rev.*, **137**, 1083–1110.

Ackerman, T. P., and G. M. Stokes, 2003: The Atmospheric Radiation Measurement program. *Phys. Today*, **56**, 38–44.

Brown, A. R., and Coauthors, 2002: Large-eddy simulation of the diurnal cycle of shallow cumulus convection over land. *Quart. J. Roy. Meteor. Soc.*, **128**, 1075–1093.

Browning, K. A., and Coauthors, 1993: The GEWEX Cloud System Study (GCSS). *Bull. Amer. Meteor. Soc.*, **74**, 387–399.

Catalano, F., and C.-H. Moeng, 2010: Large-eddy simulation of the daytime boundary layer in an idealized valley using the Weather Research and Forecasting numerical model. *Bound. -Layer Meteor.*, **137**, 49–75.

Cuijpers, J., and P. Duynkerke, 1993: Large eddy simulation of trade wind cumulus clouds. *J. Atmos. Sci.*, **50**, 3894–3908.

Deardorff, J. W., 1972: Numerical investigation of neutral and unstable planetary boundary layers. *J. Atmos. Sci.*, **29**, 91–115.

Deardorff, J. W., 1980: Stratocumulus-capped mixed layers derived from a three-dimensional model. *Bound.-Layer Meteor.*, **18**, 495–527.

Duynkerke, P. G., and Coauthors, 2004: Observations and numerical simulations of the diurnal cycle of the EUROCS stratocumulus case. *Quart. J. Roy. Meteor. Soc.*, **130**, 3269–3296.

Grabowski, W. W., X. Wu, and M. W. Moncrieff, 1996: Cloud-resolving modeling of tropical cloud systems during phase III of GATE. Part I: Two-dimensional experiments. *J. Atmos. Sci.*, **53**, 3684–3709.

Khairoutdinov, M. F., and D. A. Randall, 2003: Cloud resolving modeling of the ARM summer 1997 IOP: model formulation, results, uncertainties, and sensitivities. *J. Atmos. Sci.*, **60**, 607–625.

Lenderink, G., and Coauthors, 2004: The diurnal cycle of shallow cumulus clouds over land: A single-column model intercomparison study. *Quart. J. Roy. Meteor. Soc.*, **130**, 3339–3364.

Lin, Y.-L., R. D. Farley, and H. D. Orville, 1983: Bulk parameterization of the snow field in a cloud model. *J. Climate Appl. Meteor.*, **22**, 1065–1092.

Liu, G., J. Sun, and L. Yin, 2011a: Turbulence characteristics of the shear-free convective boundary layer driven by heterogeneous surface heating. *Bound.-Layer Meteor.*, **140**, 57–71.

Liu, Y., and Coauthors, 2011b: Simultaneous nested modeling from the synoptic scale to the LES scale for wind energy applications. *J. Wind Eng. Ind. Aerodyn.*, **99**, 308–319.

Lundquist, J., J. Mirocha, F. Chow, B. Kosovic, and K. Lundquist, 2008: Simulating atmosphere flow for wind energy applications with WRF-LES. *18th symposium on Boundary layers and turbulence. American Meteorological Society, Stockholm, Sweden*, 9–13.

Moeng, C.-H., 1984: A large-eddy-simulation model for the study of planetary boundary-layer turbulence. *J. Atmos. Sci.*, **41**, 2052–2062.

Moeng, C.-H., 1986: Large-eddy simulation of a stratus-topped boundary layer. Part I: Structure and budgets. *J. Atmos. Sci.*, **43**, 2886-2900.

Moeng, C.-H., J. Dudhia, J. Klemp, and P. Sullivan, 2007: Examining two-way grid nesting for large eddy simulation of the PBL using the WRF model. *Mon. Wea. Rev.*, **135**, 2295–2311.

Neggers, R., A. Siebesma, G. Lenderink, and A. Holtslag, 2004: An evaluation of mass flux closures for diurnal cycles of shallow cumulus. *Mon. Wea. Rev.*, **132**, 2525–2538.

Randall, D., M. Khairoutdinov, A. Arakawa, and W. Grabowski, 2003a: Breaking the cloud parameterization deadlock. *Bull. Amer. Meteor. Soc.*, **84**, 1547–1564.

Randall, D., and Coauthors, 2003b: Confronting models with data: The GEWEX Cloud System Study. *Bull. Amer. Meteor. Soc.*, **84**, 455–469.

Siebesma, A. P., and J. W. M. Cuijpers, 1995: Evaluation of parametric assumptions for shallow cumulus convection. *J. Atmos. Sci.*, **52**, 650–666.

Siebesma, A. P., P. M. M. Soares, and J. Teixeira, 2007: A combined eddy-diffusivity mass-flux approach for the convective boundary layer. *J. Atmos. Sci.*, **64**, 1230–1248.

Siebesma, A. P., and Coauthors, 2003: A large-eddy simulation intercomparison study of shallow cumulus convection. *J. Atmos. Sci.*, **60**, 1201–1219.

Skamarock, W. C., and Coauthors, 2008: A description of the Advanced Research WRF version 3. NCAR Tech. Note NCAR/TN-475+STR, 113 pp.

Soares, P., P. Miranda, A. Siebesma, and J. Teixeira, 2004: An eddy-diffusivity/mass-flux parameterization for dry and shallow cumulus convection. *Quart. J. Roy. Meteor. Soc.*, **130**, 3365–3383.

Stevens, B., W. R. Cotton, G. Feingold, and C.-H. Moeng, 1998: Large-eddy simulations of strongly precipitating, shallow, stratocumulus-topped boundary layers. *J. Atmos. Sci.*, **55**, 3616-3638.

Stevens, B., and Coauthors, 2001: Simulations of trade wind cumuli under a strong inversion. *J. Atmos. Sci.*, **58**, 1870–1891.

Stevens, B., and Coauthors, 2003: Dynamics and Chemistry of Marine Stratocumulus–DYCOMS-II. *Bull. Amer. Meteor. Soc.*, **84**, 579–593.

Stevens, B., and Coauthors, 2005: Evaluation of large-eddy simulations via observations of nocturnal marine stratocumulus. *Mon. Wea. Rev.*, **133**, 1443–1462.

Stokes, G. M. and S. E. Schwartz, 1994: The Atmospheric Radiation Measurement (ARM) program: Programmatic background and design of the cloud and radiation test bed. *Bull. Amer. Meteor. Soc.*, **75**, 1201–1221.

Tao, W.-K. and M. W. Moncrieff, 2009: Multiscale cloud system modeling. *Rev. Geophys.*, **47**, RG4002.

Wang, H. and G. Feingold, 2009a: Modeling mesoscale cellular structures and drizzle in marine stratocumulus. Part I: Impact of drizzle on the formation and evolution of open cells. *J. Atmos. Sci.*, **66**, 3237–3256.

Wang, H. and G. Feingold, 2009b: Modeling mesoscale cellular structures and drizzle in marine stratocumulus. Part II: The microphysics and dynamics of the boundary region between open and closed cells. *J. Atmos. Sci.*, **66**, 3257–3275.

Wu, X., and X. Li, 2008: A review of cloud-resolving model studies of convective processes. *Adv. Atmos. Sciences*, **25**, 202–212.

Wu, X. and M. W. Moncrieff, 2001: Long-term behavior of cloud systems in TOGA COARE and their interactions with radiative and surface processes. Part III: Effects on the energy budget and SST. *J. Atmos. Sci.*, **58**, 1155–1168.

Wyant, M., and Coauthors, 2007: A single-column model intercomparison of a heavily drizzling stratocumulus-topped boundary layer. *J. Geophys. Res.*, **112**, D24204.

Xie, S., R. T. Cederwall, M. Zhang, 2004: Developing long-term single-column model/cloud system-resolving model forcing data using numerical weather prediction products constrained by surface and top of the atmosphere observations. *J. Geophys. Res.*, **109**, D011004.

Xu, K.-M. and D. A. Randall, 2001: Updraft and downdraft statistics of simulated tropical and midlatitude cumulus convection. *J. Atmos. Sci.*, **58**, 1630–1649.

Zhang, M. H., J. L. Lin, R. T. Cederwall, J. J. Yio, and S. C. Xie, 2001: Objective analysis of ARM IOP data: Method and sensitivity. *Mon. Wea. Rev.*, **129**, 295–311.

Zhu, P., 2008: Simulation and parameterization of the turbulent transport in the hurricane boundary layer by large eddies. *J. Geophys. Res.*, **113**, D17104.

Zhu, P., B. Albrecht, V. Ghate, and Z. Zhu, 2010: Multiple-scale simulations of stratocumulus clouds. *J. Geophys. Res.*, **115**, D23 201.

Zhu, P., and Coauthors, 2005: Intercomparison and interpretation of single-column model simulations of a nocturnal stratocumulus-topped marine boundary layer. *Mon. Wea. Rev.*, **133**, 2741–2758.

Tables

Table 1: Large-scale forcing applied below 1000 m for the ARM SGP case simulation.

Time (LT)	Advective heating ($K\ h^{-1}$)	Radiative heating ($K\ h^{-1}$)	Advective moistening ($K\ h^{-1}$)
0530	0.000	-0.125	0.080
0830	0.000	0.000	0.020
1130	0.000	0.000	-0.040
1430	-0.080	0.000	-0.100
1730	-0.160	0.000	-0.160
2000	-0.160	-0.100	-0.300

Figures

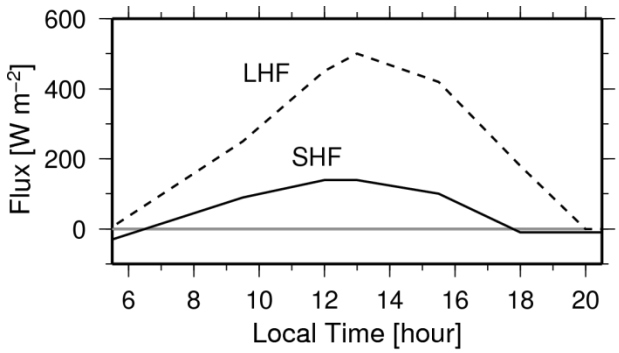

Figure 1: Time series of prescribed surface sensible heat flux (SHF; solid line) and latent heat flux (LHF; dashed line) for the ARM SGP case.

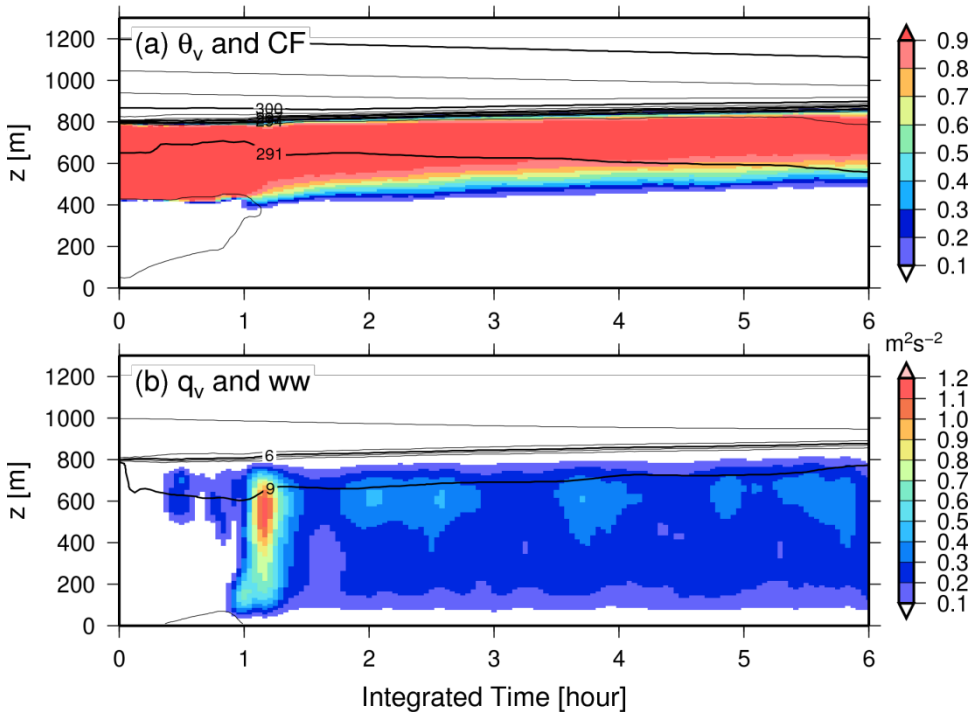

Figure 2: Time height section of (a) cloud fraction (color) and virtual potential temperature (contour), (b) variance of vertical motion (color) and water vapor mixing ratio (contour) from the WRF-FASTER simulation for the DYCOMS-II RF02 case.

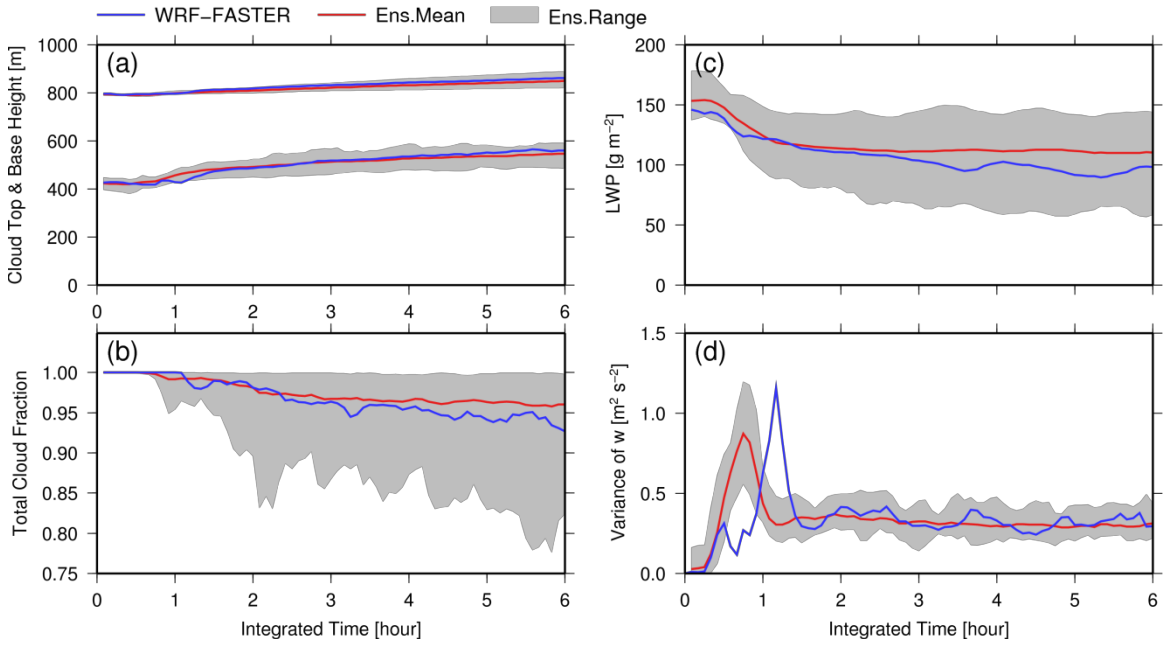

Figure 3: Time series of cloud properties in the DYCOMS-II RF02 case. (a) cloud top height (upper lines) and mean height of cloud base (lower lines). (b) Total cloud fraction. (c) Liquid water path. Solid line indicates WRF-FASTER. Dashed line and shaded area indicate ensemble mean and ensemble range of other 13 models, respectively.

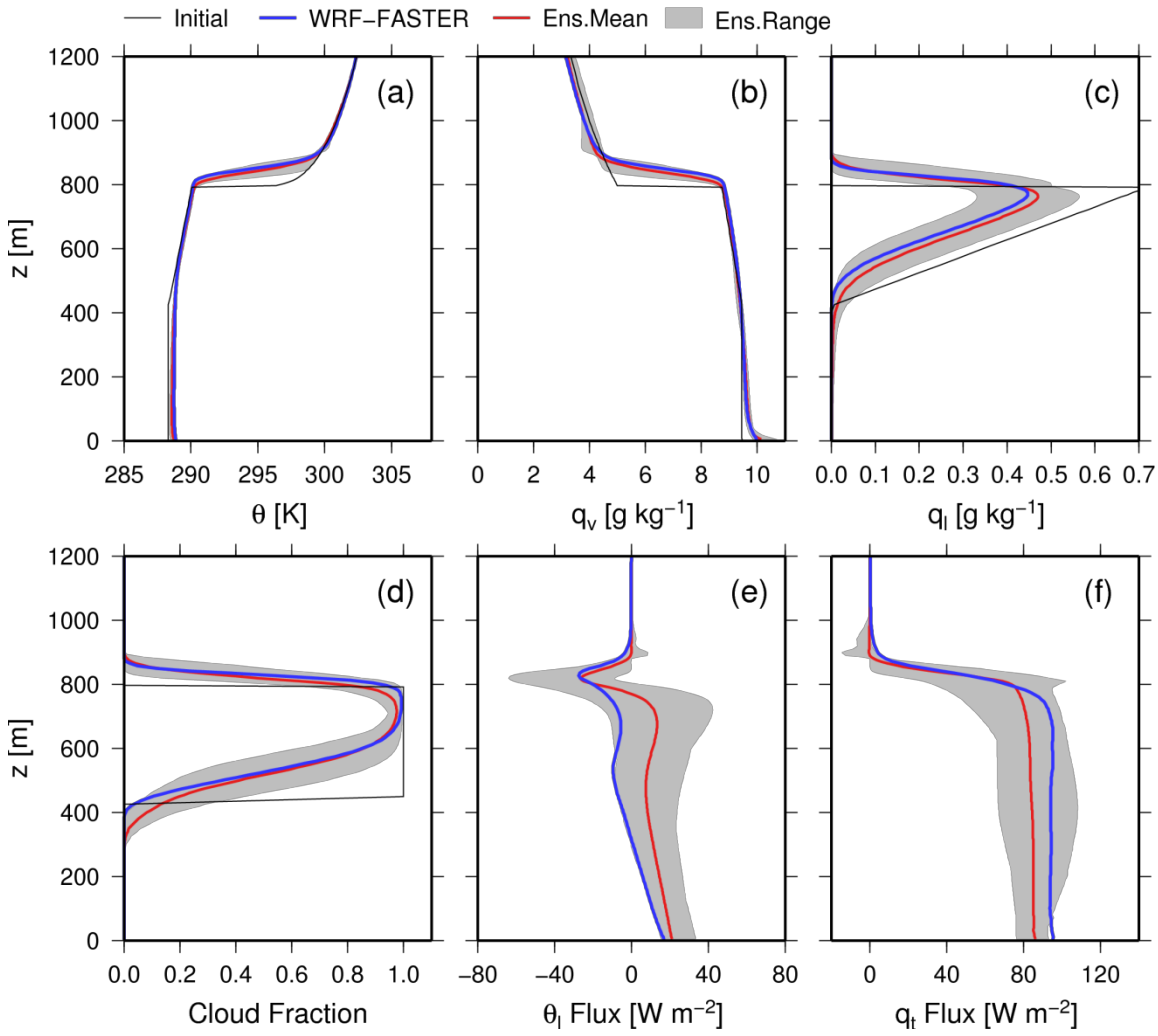

Figure 4: Vertical profiles of (a) potential temperature, (b) water vapor mixing ratio, (c) liquid water mixing ratio, (d) cloud fraction, (e) liquid water potential temperature flux, and (f) total water flux averaged over the final 4 hours of the simulation in the DYCOMS-II RF02 case. Solid line indicates WRF-FASTER. Dashed line and shaded area indicate ensemble mean and ensemble range of other 13 models, respectively. Black thin lines in the panels (a) to (d) indicate initial value.

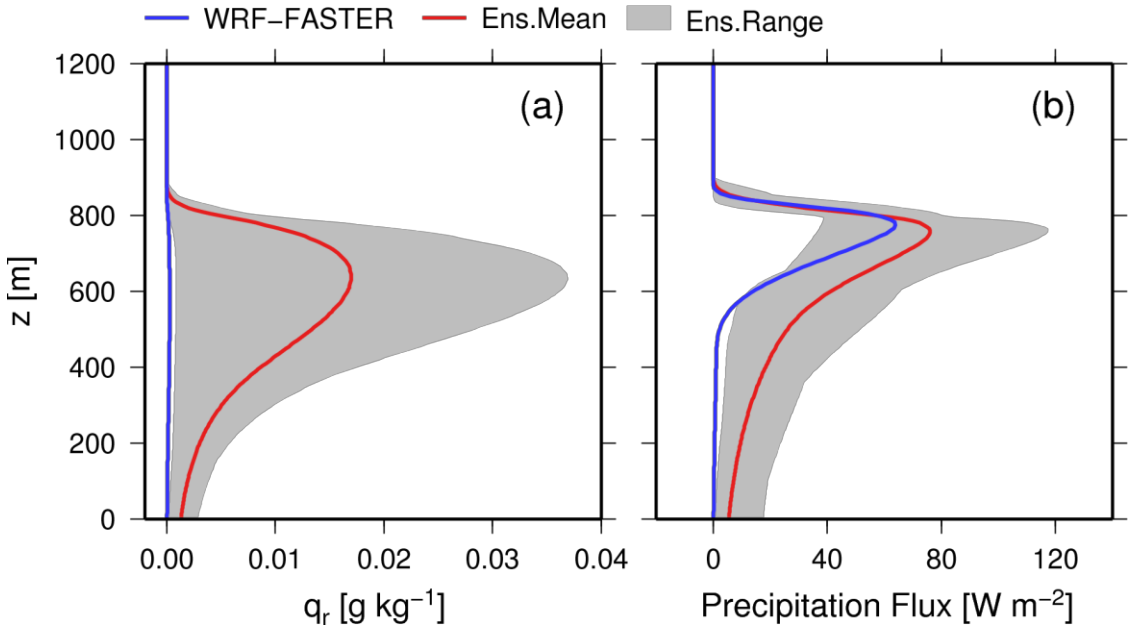

Figure 5: The same as Figure 4 but for rain water (a) and precipitation flux (b).

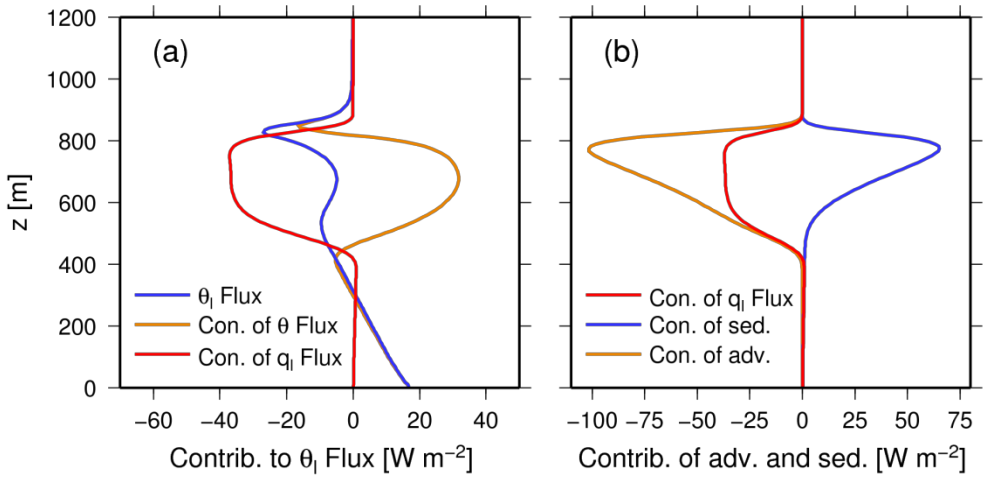

Figure 6: Vertical profiles of liquid water potential temperature flux and its components in DYCOMS-II RF02 case. (a) Liquid water potential temperature flux (solid line), contributions of potential temperature flux (dash line) and liquid water flux (dotted line). (b) Contributions of liquid water flux (dotted line; the same as (a)), sedimentation flux (solid line) and liquid water advection flux (dashed line).

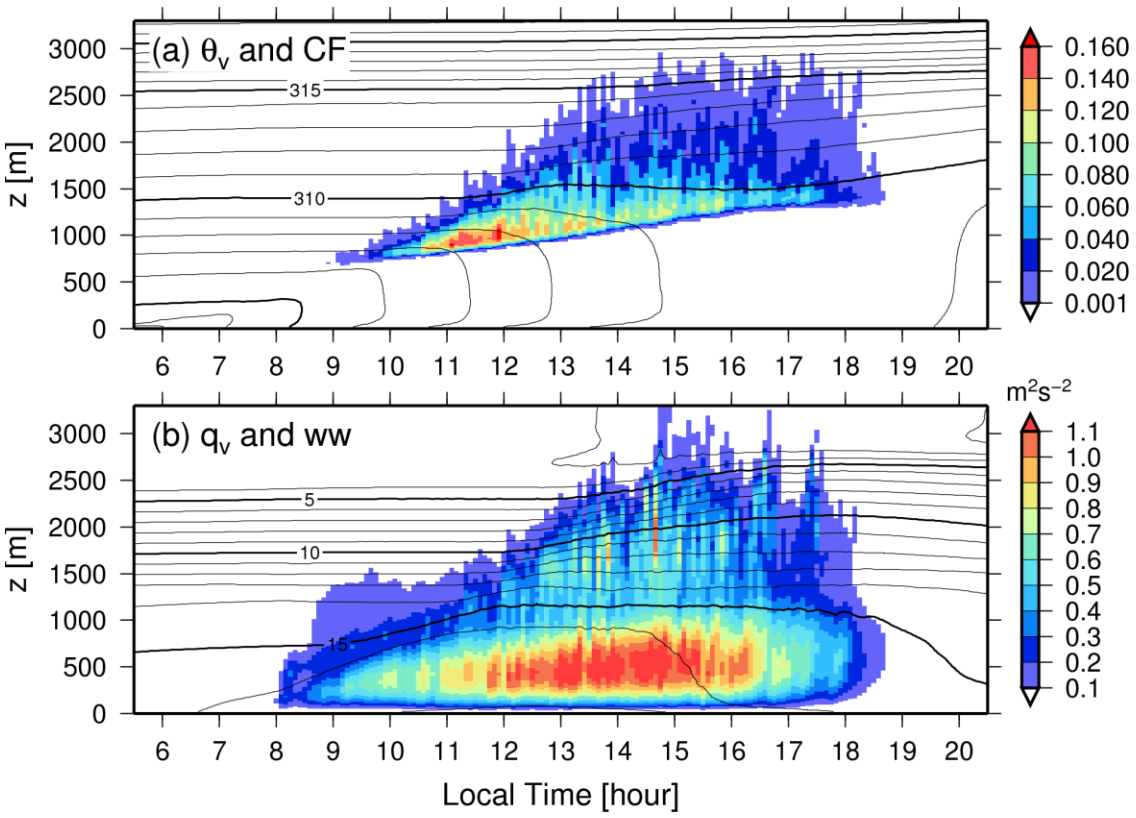

Figure 7: Time height section of (a) cloud fraction (color) and virtual potential temperature (contour), (b) variance of vertical motion (color) and water vapor mixing ratio (contour) from the WRF-FASTER simulation for the ARM SGP case.

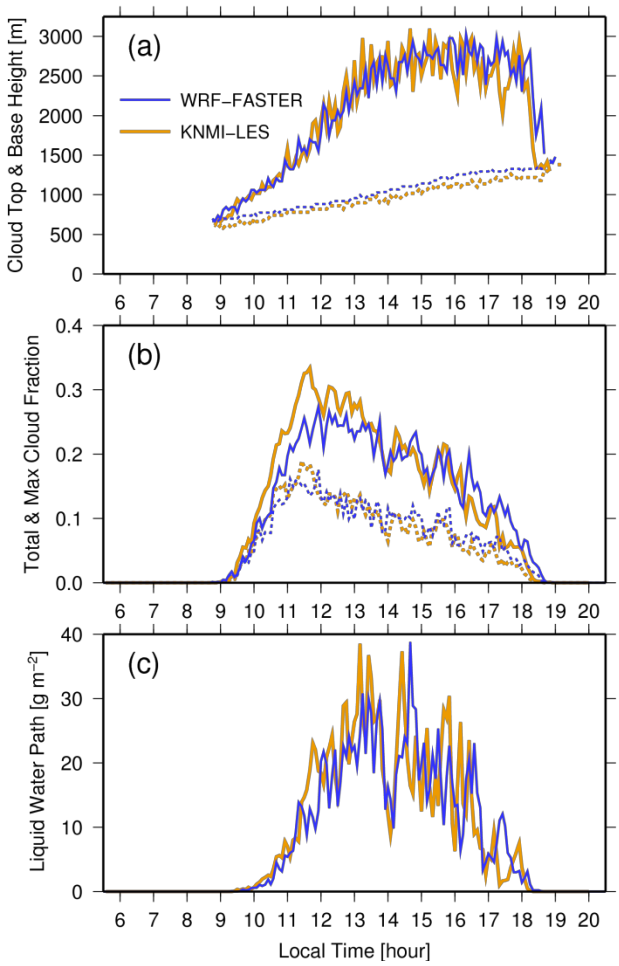

Figure 8: Time series of cloud properties in the ARM SGP case. (a) Maximum height of cloud top (solid line) and minimum height of cloud base (dotted line). (b) Total cloud fraction (solid line) and the maximum cloud fraction in the vertical profile (dotted line). (c) Liquid water path. Black and gray lines indicate WRF-FASTER and KNMI-LES, respectively.

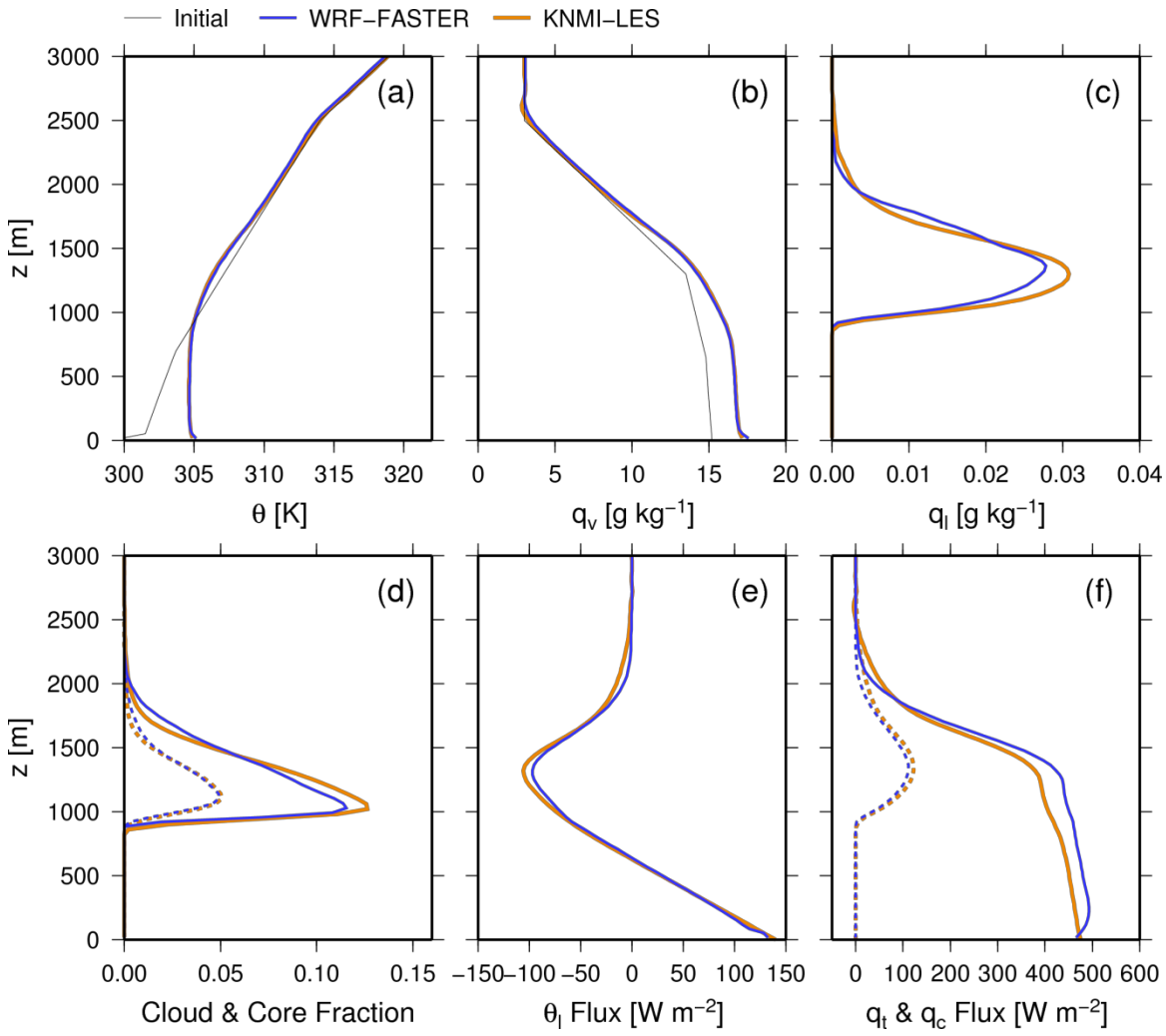

Figure 9: Vertical profiles of (a) potential temperature, (b) water vapor mixing ratio, (c) liquid water mixing ratio, (d) cloud fraction (solid line) and cloud core fraction (dashed line), (e) liquid water potential temperature flux, and (f) total water flux (solid line) and liquid water flux (dashed line) averaged over the period from 12 to 13 LT in the ARM SGP case. Blue and orange lines indicate WRF-FASTER and KNMI-LES, respectively. Black thin lines in the panels (a) and (b) indicate initial value commonly used for the both models.

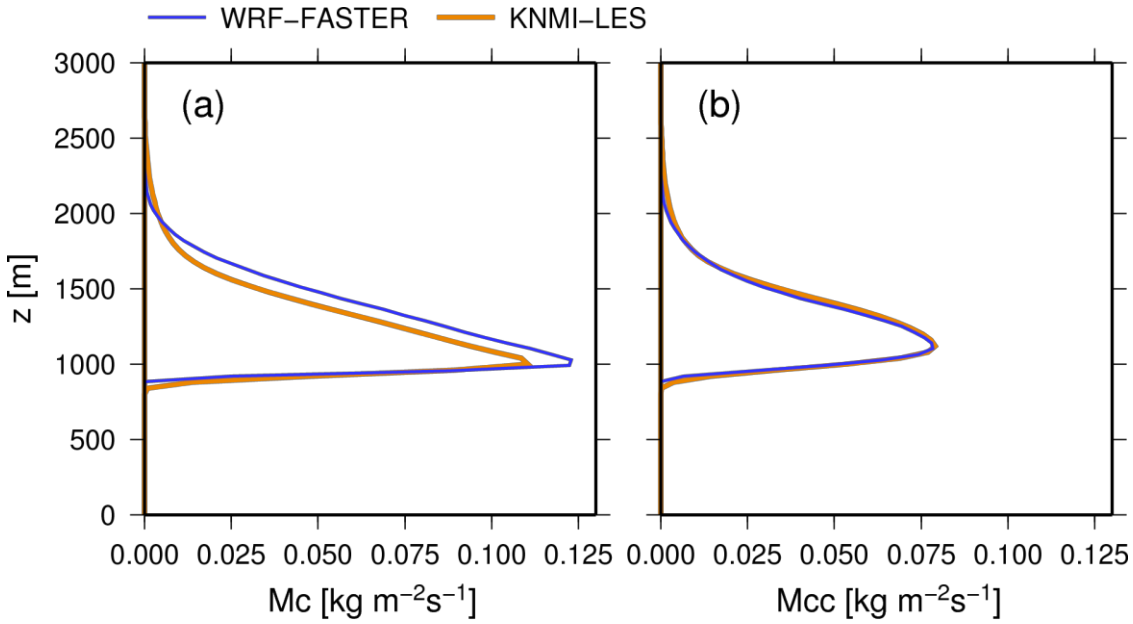

Figure 10: Vertical profiles of (a) cloud mass flux and (b) cloud core mass flux in the ARM SGP case. Black and gray lines indicate WRF-FASTER and KNMI-LES, respectively.